

Invariant-Based Finite Strain Anisotropic Material Model for Fiber-Reinforced Composites

Aamir Dean, José Reinoso, Shahab Sahraee, Benedikt Daum
and Raimund Rolfes

Abstract Short fibre reinforced plastic (SFRP) materials are intensively used in several engineering sectors due to their excellent mechanical properties and production rates. In this investigation, an invariant-based transversely isotropic elasto-plastic model for finite strain applications and its corresponding numerical treatment are presented. The current model is based on the multiplicative decomposition of the deformation gradient. The main characteristic of the formulation is the mathematical realization of the incompressibility assumption with regard to the plastic behaviour in anisotropic finite strain setting. The proposed model is complying with thermodynamic restrictions and allows robust reliable numerical simulations. The accuracy of the model is verified by comparison against experimental data, showing a very satisfactory level of agreement.

1 Introduction

Short fiber-reinforced plastics (SFRPs) are materials which exhibit excellent specific strength and stiffness ratios. These materials are especially suitable for their

A. Dean (✉) · S. Sahraee · B. Daum · R. Rolfes
Institute of Structural Analysis, Leibniz Universität Hannover, Appelstr. 9A,
30167 Hannover, Germany
e-mail: a.dean@isd.uni-hannover.de

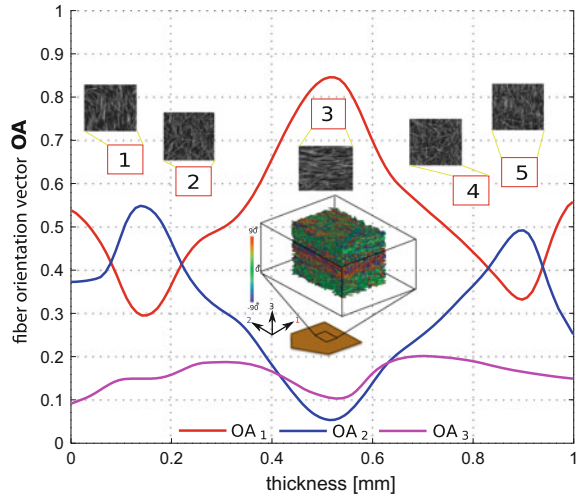
S. Sahraee
e-mail: s.sahraee@isd.uni-hannover.de

B. Daum
e-mail: b.daum@isd.uni-hannover.de

R. Rolfes
e-mail: r.rolfes@isd.uni-hannover.de

J. Reinoso
Elasticity and Strength of Materials Group, School of Engineering,
Universidad de Sevilla, Camino de Los Descubrimientos S/n, 41092 Seville, Spain
e-mail: jreinoso@us.es

Fig. 1 Micro-computed tomography of SFRP PA6GF-30 processed by injection moulding procedure



incorporation into mass production, since they usually generate low manufacturing costs. In the last years, such materials have been extensively used in several industrial sectors, in particular in the automotive industry with special interest, among many others. In practical applications, one of the most relevant production techniques to manufacture engineering products made from SFRPs, is injection molding (IM), which leads to very complex internal arrangements of the reinforcing fibers, see Fig. 1. Of particular concern are SFRPs made of a polymer matrix with reinforcing short glass fibers, which are denominated as PAXGF-y, where x and y denote the polyamide-type and the fiber content, respectively.

Due to this intricate nature, the determination of the characteristic mechanical properties, which depend on the preferential fiber orientation, is of crucial importance. This characterization can be carried out using different experimental techniques such as optical observations, radiography procedures, CT scans, among others [3, 5, 30]. In this context, in the last three decades, several studies have been conducted in order to characterize the response of SFRP composites under different loading (static and fatigue) [4, 10, 11, 18, 21] and environmental scenarios [12].

From the mechanical point of view, as a consequence of the complex heterogeneous arrangement, the effective modeling of SFRP composites faces various notable difficulties. Original investigations in this area are due to Advani and Tucker [1, 2], who envisaged a tensorial formulation to approximate the probability function regarding the fiber orientation within the domain. Alternative methodologies regard multi-scale FE-based (FE²) procedures using experimental data from 3D tomographies [15, 28, 34]. However, such FE²-methods are tremendously expensive in large-scale simulations.

In order to avoid such computational demands, phenomenological anisotropic elasto-plastic models can be considered as a modeling alternative providing mechanical accuracy and numerical efficiency. In the related literature, a high number of

investigations focused on the development of anisotropic elasto-plastic formulations under different modeling assumptions, especially within the finite deformation setting invoking the multiplicative decomposition of the deformation gradient between elastic and plastic counterparts [13, 17, 19, 20, 22, 24, 25, 32].

Inspired by these previous investigations, the current investigation presents the development of a novel phenomenological elasto-plastic invariant-based finite strain anisotropic material model for SFRP composites. Differing from previous studies [7, 8, 33], the current model incorporates the assumption of plastic incompressibility within the large deformation setting, accounting for the anisotropic character of SFRP composites through a structural tensorial representation. The proposed formulation is derived following a thermodynamic framework, which guarantees its consistency. On the computational side, specific aspects regarding the numerical integration of the evolution equations corresponding to the internal variables and the consistent elasto-plastic tangent moduli are outlined. Finally, the predictive capability of the model is examined through several applications.

The manuscript is organized as follows. Section 2 describes the basic arguments with regard to the continuous formulation. The constitutive model according to invariant-based formulation is given in Sect. 3. The numerical treatment of the proposed model within the context of a fully implicit nonlinear Finite Element Method (FEM) is addressed in Sect. 4. The applicability of the material model is confirmed through the examination of the experimental-numerical correlation regarding several applications (Sect. 5). Finally, the main conclusions of the current investigation are drawn in Sect. 6.

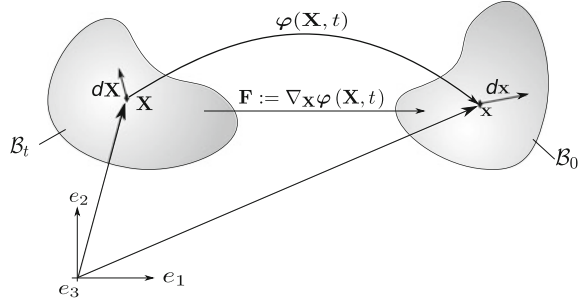
2 Continuous Formulation

This section presents the fundamental aspects of the novel finite deformation model for SFRP composites within the finite deformation setting. The current formulation uses an invariant-based formulation to account for the directional character of SFRPs composites using a tensorial representation in line with [7–9].

2.1 Basic Kinematics

Following the standard setting of finite inelasticity, consider a continuous three dimensional body which occupies the reference placement $\mathcal{B}_0 \subset \mathbb{R}^3$, where $\mathbf{X} \in \mathcal{B}_0$ denotes an arbitrary material point in this configuration. At time $t \in \mathbb{R}_+$, the corresponding spatially deformed configuration is denoted by $\mathcal{B}_t \subset \mathbb{R}^3$. An individual material point at time t is located at the position $\mathbf{x} \in \mathcal{B}_t$. Both configurations are related via the nonlinear deformation mapping $\varphi : \mathcal{B}_0 \times [0, t] \rightarrow \mathbb{R}^3$, where $[0, t]$ denotes the time interval elapsed. This operator maps the reference material points

Fig. 2 Motion of a continuum body: reference and current configurations, the nonlinear mapping concept, deformation gradient



($\mathbf{X} \in \mathcal{B}_0$) onto the current material points ($\mathbf{x} \in \mathcal{B}_t$), i.e. $\mathbf{x} = \boldsymbol{\varphi}(\mathbf{X}, t)$, see Fig. 2. Therefore, the displacement vector at material point level is given by: $\mathbf{u} := \mathbf{x} - \mathbf{X}$.

As a measure of the deformation process experienced by the body, we consider the deformation gradient \mathbf{F} that represents the linear mapping between tangent vectors in the reference and current configurations:

$$\mathbf{F} := \frac{\partial \boldsymbol{\varphi}(\mathbf{X}, t)}{\partial \mathbf{X}} = \mathbf{1} + \mathbf{H}(\mathbf{X}, t); \quad \mathbf{H}(\mathbf{X}, t) = \nabla_{\mathbf{X}} \mathbf{u}(\mathbf{X}, t), \quad (1)$$

where $\mathbf{1}$ is the second-order identity tensor and $\nabla_{\mathbf{X}}[\bullet]$ identifies the gradient of the quantity \bullet with respect to the reference setting. The Jacobian of the transformation $J = \det[\mathbf{F}]$ has to satisfy $J \geq 0$. The polar decomposition of the deformation gradient is given by $\mathbf{F} = \mathbf{R}\mathbf{U}$, where \mathbf{R} and \mathbf{U} respectively denote the rotation tensor and the stretch tensor.

The definition of the symmetric right and left Cauchy-Green deformation tensors, \mathbf{C} and \mathbf{b} , respectively, and the Green-Lagrange strain tensor, \mathbf{E} , is given by:

$$\mathbf{C} := \mathbf{F}^T \mathbf{F}; \quad \mathbf{b} := \mathbf{F} \mathbf{F}^T; \quad \mathbf{E} := \frac{1}{2} [\mathbf{C} - \mathbf{1}], \quad (2)$$

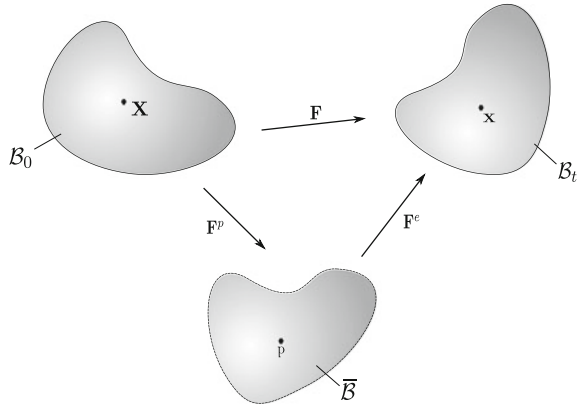
A central point of the proposed constitutive model for SFRPs is the adoption of the classical multiplicative decomposition of the deformation gradient into elastic and plastic counterparts considering a stress-free intermediate configuration $\tilde{\mathcal{B}}$ [27], see Fig. 3:

$$\mathbf{F} = \mathbf{F}^e \mathbf{F}^p. \quad (3)$$

Based on Eq. (3), the elastic part \mathbf{E}^e of the Green-Lagrange strain tensor in the intermediate configuration is defined as:

$$\mathbf{E}^e = \frac{1}{2} [\mathbf{C}^e - \mathbf{1}], \quad (4)$$

Fig. 3 Intermediate configuration definition: multiplicative decomposition of the deformation gradient $\mathbf{F} = \mathbf{F}^e \mathbf{F}^p$ for large deformation elasto-plasticity



where $\mathbf{C}^e := \mathbf{F}^{eT} \mathbf{F}^e$ is the elastic right Cauchy-Green strain tensor. Finally, the assumption of plastic incompressibility requires the satisfaction of the following constraint:

$$\det \mathbf{F}^p = 1. \quad (5)$$

2.2 Balance Laws

The local form of the balance of linear momentum, which governs the initial boundary value problem (IBVP) of the body's deformation process, takes the following form neglecting the inertia terms:

$$\text{DIV} \mathbf{P}(\mathbf{X}, t) + \tilde{\mathbf{Y}}(\mathbf{X}) = \mathbf{0}, \quad (6)$$

where the operator $\text{DIV}[\bullet]$ stands for the divergence of the tensor field \bullet with respect to the reference frame, $\tilde{\mathbf{Y}}$ denotes the body forces (per unit reference volume) of the continuum. In Eq. (6), \mathbf{P} is the first Piola-Kirchhoff stress tensor, which can be associated with the symmetric second Piola-Kirchhoff stress tensor \mathbf{S} as follows: $\mathbf{P} = \mathbf{F} \mathbf{S}$. The complete (IBVP) is defined with the suitable boundary conditions in terms of displacements $\tilde{\mathbf{u}} : \Gamma_u \times [0, t] \rightarrow \mathbb{R}^3$ and nominal tractions $\tilde{\mathbf{T}} : \Gamma_t \times [0, t] \rightarrow \mathbb{R}^3$ which are prescribed on the corresponding subsets of the body boundary.

The balance of angular momentum implies the symmetry condition of the second Piola-Kirchhoff stress tensor in the reference configuration $\mathbf{S} = \mathbf{S}^T$. The balance of energy (first law of thermodynamics) postulates the energy preservation during the deformation process. The material version of the balance of energy reads:

$$\rho_0 \dot{e} = \mathbf{S} : \dot{\mathbf{E}} + R - \text{DIV} [\mathbf{Q}], \quad (7)$$

where e denotes the specific internal energy, ρ_0 is the reference density, \mathbf{Q} is the reference heat flux, and finally R refers to the internal heat source measured per unit reference volume.

The thermodynamic consistency of the proposed formulation is assessed via the evaluation of the Clausius-Planck inequality [31]:

$$\mathcal{D}_{\text{int}} = \mathbf{S} : \dot{\mathbf{E}} - \dot{e} + \vartheta \dot{\eta} \geq 0, \quad (8)$$

where \mathcal{D}_{int} is the local dissipation per unit of volume, $\dot{\mathbf{E}}$ stands for the material time derivative of the Green-Lagrange strain tensor. The symbol \dot{e} identifies the time derivative of the specific internal energy, whereas ϑ and $\dot{\eta}$ denote the temperature and the time derivative of the entropy of the system η . Under isothermal conditions and recalling the Legendre transformation [16], Eq. (8) is reduced to:

$$\mathcal{D}_{\text{int}} = \mathbf{S} : \dot{\mathbf{E}} - \dot{\Psi} \geq 0, \quad (9)$$

where Ψ is the Helmholtz free energy function that characterizes the material response.

3 Constitutive Model: Invariant-Based Formulation

3.1 Fundamental Aspects

The mechanical performance of SFRP composites exhibits relevant nonlinear effects along the deformation process prior to failure with a pronounced anisotropic character. This complex behavior arises from the molding flow production process which is employed for manufacturing purposes leading to nonuniform fiber distribution within the specimen. From the modeling standpoint, this directional dependency can be accounted for by means of a purely phenomenological anisotropic plasticity model at finite strains [7–9]. Assuming a tensorial representation of such anisotropic effects, we define a second-order structural tensor \mathbf{A} in the reference configuration:

$$\mathbf{A} := \mathbf{a} \otimes \mathbf{a}, \quad (10)$$

where \mathbf{a} is the direction with the highest aligned fiber content, coinciding with the molding direction. Consequently, the material response is invariant (symmetry transformations) with respect to: (i) arbitrary rotations around \mathbf{a} , (ii) reflections at planes parallel to \mathbf{a} and, (iii) planes whose normal vector is aligned with \mathbf{a} [6, 29].

Relying on the previous considerations, the Helmholtz free energy function Ψ that characterizes the mechanical response of SFRPs is assumed to allow the following decomposition:

$$\Psi(\mathbf{E}^e, \boldsymbol{\zeta}, \mathbf{A}) = \Psi^e(\mathbf{E}^e, \mathbf{A}) + \Psi^p(\boldsymbol{\zeta}, \mathbf{A}), \quad (11)$$

where $\Psi^e(\mathbf{E}^e, \mathbf{A})$ and $\Psi^p(\boldsymbol{\zeta}, \mathbf{A})$ identify the elastic and plastic counterparts, respectively, and $\boldsymbol{\zeta}$ stands for the vector of internal variables that trigger the evolution of the inelastic response. The anisotropic mechanical behavior is modeled through the consideration of the following irreducible integrity basis of invariants $\mathcal{P} := [J_1, \dots, J_4]$. The invariants J_1 and J_2 are given by:

$$J_1 := \text{tr}[\mathbf{E}^e], \quad J_2 := \text{tr}\left[(\mathbf{E}^e)^2\right], \quad (12)$$

whereas the mixed invariants J_3 and J_4 render:

$$J_3 := \text{tr}[\mathbf{A}\mathbf{E}^e], \quad J_4 := \text{tr}\left[\mathbf{A}(\mathbf{E}^e)^2\right]. \quad (13)$$

Then, assuming a quadratic form, the elastic free energy function can be expressed as [8]:

$$\Psi^e(\mathbf{E}^e, \mathbf{A}) = \frac{\lambda}{2} J_1^2 + \mu_T J_2 + \alpha J_3 J_1 + 2(\mu_L - \mu_T) J_4 + \frac{\beta}{2} J_3^2 = \frac{1}{2} \mathbf{E}^e : \mathbb{C}^e : \mathbf{E}^e, \quad (14)$$

where $\lambda, \mu_L, \mu_T, \alpha, \beta$ identify the elastic constants [33].

The second Piola-Kirchhoff stress tensor \mathbf{S} and its corresponding elasticity tensor \mathbb{C}^e adopt the form:

$$\mathbf{S}(\mathbf{E}^e, \mathbf{A}) := \partial_{\mathbf{E}^e} \Psi = \lambda \text{tr}[\mathbf{E}^e] \mathbf{1} + 2\mu_T \mathbf{E}^e + \alpha (\text{tr}[\mathbf{A}\mathbf{E}^e] + \text{tr}[\mathbf{E}^e \mathbf{A}]) \mathbf{1} + 2(\mu_L - \mu_T) (\mathbf{E}^e \mathbf{A} + \mathbf{A}\mathbf{E}^e) + \beta \text{tr}[\mathbf{A}\mathbf{E}^e] \mathbf{A} \quad (15)$$

$$\mathbb{C}^e := \frac{\partial^2 \Psi^e}{\partial \mathbf{E}^e \otimes \partial \mathbf{E}^e} = \lambda \mathbf{1} \otimes \mathbf{1} + 2\mu_T \mathbb{I} + \alpha (\mathbf{1} \otimes \mathbf{A} + \mathbf{A} \otimes \mathbf{1}) + 2(\mu_L - \mu_T) \mathbb{I}_{\mathbf{A}} + \beta \mathbf{A} \otimes \mathbf{A}, \quad (16)$$

where \mathbb{I} stands for the fourth-order symmetric identity tensor and $\mathbb{I}_{\mathbf{A}}$ takes the form:

$$\mathbb{I}_{\mathbf{A}} \Rightarrow \mathbb{I}_{\mathbf{A},ijkl} = \mathbf{A}_{im} \mathbb{I}_{jmkl} + \mathbf{A}_{jm} \mathbb{I}_{mikl}. \quad (17)$$

Exploiting the multiplicative decomposition of the deformation gradient, Eq. (3), the internal dissipation under isothermal conditions yields:

$$\mathcal{D}_{\text{int}} = \mathbf{S} : \left(\frac{1}{2} \mathbf{F}^{pT} \dot{\mathbf{C}}^e \mathbf{F}^p + \mathbf{F}^{pT} (\mathbf{C}^e \mathbf{L}^p)_{\text{sym}} \mathbf{F}^p \right) - \dot{\Psi} \geq 0, \quad (18)$$

where the operator $(\bullet)_{\text{sym}}$ stands for the symmetric part of the tensor field \bullet . The symbol $\mathbf{L}^p = \dot{\mathbf{F}}^p \mathbf{F}^{p-1}$ identifies the plastic velocity gradient, which can be split into its symmetric \mathbf{D}^p (plastic deformation rate) and skew-symmetric \mathbf{W}^p (plastic material spin) parts:

$$\mathbf{L}^p = \mathbf{D}^p + \mathbf{W}^p. \quad (19)$$

The insertion of the previous definitions into Eq. (18) yields:

$$\mathcal{D}_{\text{int}} = \frac{1}{2} \bar{\mathbf{S}} : \dot{\mathbf{C}}^e + \bar{\mathbf{S}} : (\mathbf{C}^e \mathbf{L}^p)_{\text{sym}} - \dot{\Psi}^e - \dot{\Psi}^p \geq 0, \quad (20)$$

where $\bar{\mathbf{S}} = \mathbf{F}^p \mathbf{S} \mathbf{F}^{pT}$ identifies the second Piola-Kirchhoff stress tensor counterpart in the intermediate configuration. The result is:

$$\mathcal{D}_{\text{int}} = \left(\frac{1}{2} \bar{\mathbf{S}} - \frac{\partial \Psi^e}{\partial \mathbf{C}^e} \right) : \dot{\mathbf{C}}^e + (\mathbf{C}^e \bar{\mathbf{S}}) : \mathbf{L}^p - \dot{\Psi}^p \geq 0. \quad (21)$$

Based on the previous procedure, the restriction with regard to the local internal dissipation in order to fulfill the second law of thermodynamics reads:

$$\mathcal{D}_{\text{int}} = \bar{\mathbf{\Sigma}} : \mathbf{L}^p - \dot{\Psi}^p \geq 0, \quad (22)$$

where $\bar{\mathbf{\Sigma}} = \mathbf{C}^e \bar{\mathbf{S}}$ identifies the so-called Mandel stress tensor.

3.2 Transversely Isotropic Yield Function

This section outlines the construction of the transversely isotropic yield function which characterizes the plastic locus of the current anisotropic finite strain elasto-plastic model [7, 8]. The elastic domain \mathbb{E} is defined in terms of the symmetric part of Mandel stress tensor $\bar{\mathbf{\Sigma}}_s$ as follows:

$$\mathbb{E} = \{ (\boldsymbol{\zeta}, \bar{\varepsilon}^p) \mid f(\bar{\mathbf{\Sigma}}_s, \mathbf{A}, \bar{\varepsilon}^p) \leq 0 \}, \quad (23)$$

where $\bar{\varepsilon}^p$ identifies the equivalent plastic strain (hardening variable). The evolution equation of $\bar{\varepsilon}^p$ reads:

$$\dot{\bar{\varepsilon}}^p = \sqrt{\frac{2}{3} \mathbf{D}^p : \mathbf{D}^p}. \quad (24)$$

The proposed pressure-dependent, transversely isotropic and asymmetric yield surface $f(\bar{\mathbf{\Sigma}}_s, \mathbf{A}, \bar{\varepsilon}^p) \leq 0$ follows a quadratic construction, which can be expressed in terms of the invariant set as:

$$f(\bar{\mathbf{\Sigma}}_s, \mathbf{A}, \bar{\varepsilon}^p) = \zeta_1 I_1 + \zeta_2 I_2 + \zeta_3 I_3 + \zeta_4 I_3^2 + \zeta_5 I_4 + \zeta_6 I_4^2 - 1 \leq 0, \quad (25)$$

where I_i ($i = 1, \dots, 4$) denote the integrity basis (invariants) taking the form:

$$I_1 := \text{tr} \left[\left(\bar{\mathbf{\Sigma}}_s^{\text{pind}} \right)^2 \right] - \text{tr} \left[\mathbf{A} \left(\bar{\mathbf{\Sigma}}_s^{\text{pind}} \right)^2 \right]; \quad I_2 := \text{tr} \left[\mathbf{A} \left(\bar{\mathbf{\Sigma}}_s^{\text{pind}} \right)^2 \right]; \quad (26)$$

$$I_3 := \text{tr} [\bar{\boldsymbol{\Sigma}}_s] - \text{tr} [\mathbf{A} \bar{\boldsymbol{\Sigma}}_s]; \quad I_4 := \frac{3}{2} \text{tr} [\mathbf{A} \bar{\boldsymbol{\Sigma}}_s^{\text{dev}}]. \quad (27)$$

In Eqs. (26)–(27), $\bar{\boldsymbol{\Sigma}}_s^{\text{dev}}$ denotes the deviatoric part of the symmetric Mandel stress tensor and $\bar{\boldsymbol{\Sigma}}_s^{\text{pind}}$ is the basic stress that induces plasticity [33]:

$$\bar{\boldsymbol{\Sigma}}_s^{\text{pind}} = \bar{\boldsymbol{\Sigma}}_s - \frac{1}{2} (\text{tr} [\bar{\boldsymbol{\Sigma}}_s] - \text{tr} [\mathbf{A} \bar{\boldsymbol{\Sigma}}_s]) \mathbf{1} + \frac{1}{2} (\text{tr} [\bar{\boldsymbol{\Sigma}}_s] - 3 \text{tr} [\mathbf{A} \bar{\boldsymbol{\Sigma}}_s]) \mathbf{A}. \quad (28)$$

In condensed format, the yield function renders:

$$f(\bar{\boldsymbol{\Sigma}}_s, \mathbf{A}, \bar{\varepsilon}^p) = \frac{1}{2} \bar{\boldsymbol{\Sigma}}_s : \mathbb{K} : \bar{\boldsymbol{\Sigma}}_s + \mathbf{L} : \bar{\boldsymbol{\Sigma}}_s - 1 \leq 0, \quad (29)$$

with

$$\mathbb{K} := \zeta_1 \mathbb{P}^{\text{pind}} + (\zeta_2 - \zeta_1) \mathbb{P}_{\mathbf{A}}^{\text{pind}} + 2\zeta_4 (\mathbf{1} - \mathbf{A}) \otimes (\mathbf{1} - \mathbf{A}) + \frac{9}{2} \zeta_6 \mathbf{A}^{\text{dev}} \otimes \mathbf{A}^{\text{dev}}, \quad (30)$$

$$\mathbf{L} := \zeta_3 (\mathbf{1} - \mathbf{A}) + \frac{3}{2} \zeta_5 \mathbf{A}^{\text{dev}}, \quad (31)$$

$$\mathbb{P}^{\text{pind}} := \mathbb{I} - \frac{1}{2} (\mathbf{1} \otimes \mathbf{1}) + \frac{1}{2} (\mathbf{1} \otimes \mathbf{A} + \mathbf{A} \otimes \mathbf{1}) - \frac{3}{2} \mathbf{A} \otimes \mathbf{A}, \quad (32)$$

$$\mathbb{P}_{\mathbf{A}}^{\text{pind}} \Rightarrow \mathbb{P}_{\mathbf{A},ijkl}^{\text{pind}} = \mathbf{A}_{im} \mathbb{P}_{mjkl}^{\text{pind}} + \mathbf{A}_{mj} \mathbb{P}_{imkl}^{\text{pind}}, \quad (33)$$

\mathbf{A}^{dev} being the deviatoric part of \mathbf{A} .

Figure 4 portrays a schematic 3D representation of the previous yield function in the principle stress and invariant space where an appropriate convex form can be observed.

Finally, the six parameters ζ_i ($\bar{\varepsilon}^p$), ($i = 1, \dots, 6$) and their corresponding invariants are correlated with different loading states. In particular, the following physical interpretation of these parameters can be regarded [7, 8]: (1) ζ_1 concerns transverse shear loading states, (2) ζ_2 is associated with in-plane shear loadings, (3) ζ_3 and ζ_4 account for loading states transverse to the fiber direction, and finally (4) ζ_5 and ζ_6 involve the material response subjected to longitudinal loading aligned with the fiber direction.

3.3 Plastic Potential Function

Recalling the plastic incompressibility assumption, Eq. (5), the current model introduces the definition of a non-associative flow rule. The use of a non-associative flow rule results from the need for an accurate capturing of plastic deformations [8].

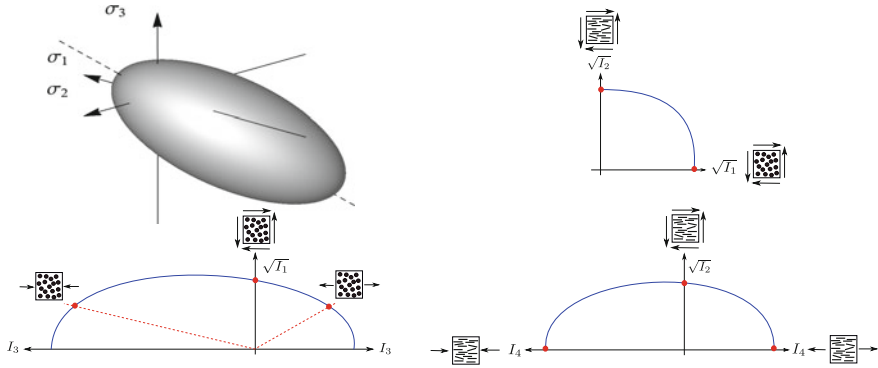


Fig. 4 Transversely isotropic yield function: 3D representation in the principal stress space and cross sections in the invariant space

Accordingly, the following anisotropic plastic potential function $g = g(\bar{\Sigma}_s, \mathbf{A})$ is formulated:

$$g(\bar{\Sigma}_s, \mathbf{A}) = \iota_1 \bar{I}_1 + \iota_2 \bar{I}_2 - 1 \leq 0, \quad (34)$$

where \bar{I}_1 and \bar{I}_2 are the integrity basis (invariants):

$$\bar{I}_1 := \text{tr} \left[\left(\bar{\Sigma}_s^{dev} \right)^2 \right]; \quad \bar{I}_2 := \text{tr} \left[\mathbf{A} \left(\bar{\Sigma}_s^{dev} \right)^2 \right], \quad (35)$$

where ι_1 and ι_2 denote the plastic potential parameters [7]. In condensed format, g yields:

$$g(\bar{\Sigma}_s, \mathbf{A}) = \frac{1}{2} \bar{\Sigma}_s : \mathbb{M} : \bar{\Sigma}_s - 1 \leq 0, \quad (36)$$

with

$$\mathbb{M} := 2\iota_1 \mathbb{I}^{dev} + \iota_2 \mathbb{I}_{\mathbf{A}}^{dev}; \quad \mathbb{I}^{dev} := \mathbb{I} - \frac{1}{3} \mathbf{1} \otimes \mathbf{1}; \quad \mathbb{I}_{\mathbf{A}}^{dev} \Rightarrow \mathbb{I}_{\mathbf{A},klmn}^{dev} = \mathbf{A}_{ij} \left(\mathbb{I}_{jsmn}^{dev} \mathbb{I}_{sikl}^{dev} + \mathbb{I}_{jskl}^{dev} \mathbb{I}_{simn}^{dev} \right). \quad (37)$$

Figure 5 depicts a cross section of the plastic potential in the invariant space and a 3D representation in the principal stress space.

3.4 Evolution Equations of the Internal Variables

Recalling the maximum energy dissipation principle [27] and using the non-associative flow rule introduced in Sect. 3.3, the evolution equations of the internal variables, namely the plastic velocity gradient \mathbf{L}^p and the hardening variable $\bar{\varepsilon}^p$, are defined in the following.

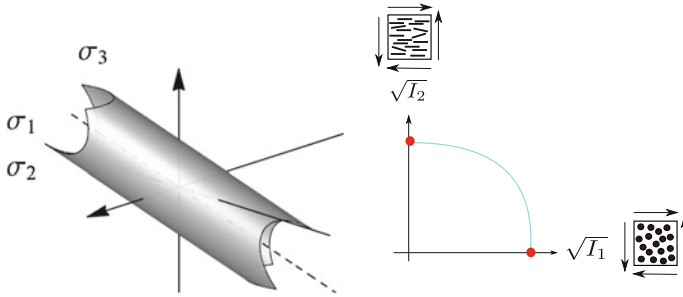


Fig. 5 Plastic potential function: 3D representation in the principal stress space and cross sections in the invariant space

Regarding the plastic velocity gradient, its corresponding evolution equation reads:

$$\mathbf{L}^p = \mathbf{D}^p = \dot{\gamma} \frac{\partial g(\bar{\boldsymbol{\Sigma}}_s, \mathbf{A})}{\partial \bar{\boldsymbol{\Sigma}}_s} = \dot{\gamma} \mathbf{n}_g \quad \text{with} \quad \mathbf{n}_g = \mathbb{M} : \bar{\boldsymbol{\Sigma}}_s. \quad (38)$$

Referring to the equivalent plastic strain, the evolution equation takes the form:

$$\dot{\bar{\varepsilon}}^p = \sqrt{\frac{2}{3} \mathbf{D}^p : \mathbf{D}^p} = \dot{\gamma} \sqrt{\frac{2}{3}} \|\mathbf{n}_g\|, \quad (39)$$

$\dot{\gamma}$ identifying the so-called plastic multiplier.

It is worth mentioning that the symmetric part of the Mandel stress tensor is the unique operator that enters into the plastic potential function, and, therefore, evolution of the plastic material spin \mathbf{W}^p vanishes. Consequently, the constitutive model is invariant with respect to any arbitrary rigid body rotation $\bar{\mathbf{Q}}$.

Finally, the standard Kuhn-Tucker loading/unloading conditions, which ensure the coherence of the model, take the form:

$$\dot{\gamma} \geq 0; \quad f(\bar{\boldsymbol{\Sigma}}_s, \mathbf{A}, \bar{\varepsilon}^p) \leq 0; \quad \dot{\gamma} f(\bar{\boldsymbol{\Sigma}}_s, \mathbf{A}, \bar{\varepsilon}^p) = 0. \quad (40)$$

Finally, the consistency condition is given by:

$$\dot{\gamma} \dot{f}(\bar{\boldsymbol{\Sigma}}_s, \mathbf{A}, \bar{\varepsilon}^p) = 0. \quad (41)$$

3.5 Parameter Identification

The yield function Eq. (25) and the plastic potential Eq. (34) are matched to actual materials via the coefficients of the invariants ζ_i and t_i , respectively. A detailed description of the procedure to adjust these coefficients to experimental data is given in [7, 33], and the main points are outlined below.

The coefficients ζ_i control the size and shape of the elastic region as a function of the equivalent plastic strain variable $\bar{\epsilon}^p$. For each coefficient, the relation $\zeta_i(\bar{\epsilon}^p)$ should be determined from an independent experiment. Typically, this relation is obtained from experiments realizing a simple, controlled stress state with only one nonzero stress component $Y_j(\bar{\epsilon}^p)$ while yielding. In the present case, the following tests can be employed for this purpose: (i) in-plane shear test, (ii) transverse shear test, (iii) uniaxial longitudinal tension and (iv) compression tests, and (v) uniaxial transverse tension and (vi) compression tests. The relation $\zeta_i(Y_{ft}, Y_{fc}, Y_{tt}, Y_{tc}, Y_{is}, Y_{ts})$ can then be derived from inserting the stress tensor corresponding to the test in Eq. (25) and setting $f = 0$. The symbols Y_{ft} , Y_{fc} , Y_{tt} and Y_{tc} represent the uniaxial yield stresses in fiber direction, first index ‘f’, and transverse direction, first index ‘t’. The second index indicates tension (‘t’) or compression (‘c’). The symbols Y_{is} and Y_{ts} stand for the transverse and in-plane shear yield stresses, respectively.

To comply with the maximum dissipation principle, the yield surface must be convex, which imposes a restriction to the allowable relations $\zeta_i(\bar{\epsilon}^p)$ which can be used in Eq. (25). Convexity is ensured, if the quadratic term in Eq. (29) is positive definite, and this requirement can be reduced to an inequality in terms of the yield stresses, c.f. Eq. (42), which must hold for any $\bar{\epsilon}^p$.

$$Y_{ft}Y_{fc}(4Y_{ts}^2 - Y_{tt}Y_{tc}) \geq Y_{tc}Y_{ts}^2Y_{tt} \quad (42)$$

The main motivation to adopt a non-associated plasticity scheme is the ability to optimize the plastic deformation behaviour independently of the yield strengths. The form of the plastic potential adopted in Eq. (34) has two adjustable coefficients ι_i . However, one of them is a scaling parameter associated with the size of the potential surface. The size of the plastic potential has no inherent meaning and can be set at will. This leaves only one remaining parameter to match with experimental data in the present case, but, if needed, extra parameters could be introduced by choosing a more complex form of g . Here, ι_1 is arbitrarily set to unity and ι_2 is used to enforce a certain plastic Poisson’s ratio $\nu_{23}^p = \epsilon_{22}^p/\epsilon_{33}^p$ for uniaxial transverse tension.

$$\iota_1 = 1, \quad \nu_{23}^p := \frac{\frac{\partial g}{\partial \sigma_{22}}}{\frac{\partial g}{\partial \sigma_{33}}} \Big|_{\sigma_{33}=Y_{tt}} = \frac{-3\iota_1 + \iota_2}{6\iota_1 + \iota_2} \Rightarrow \iota_2 = \frac{3 + 6\nu_{23}^p}{-1 + \nu_{23}^p}$$

Unlike the yield function coefficients, usually no evolution of ι_i with respect to the equivalent plastic strain is considered.

4 Numerical Treatment

This section presents the numerical treatment of the constitutive model given in Sect. 3. The construction of a numerical scheme for the solution of the initial boundary value problem (IBVP) associated involves two general steps [8]: (i) the local

integration of the transversely isotropic elasto-plastic model via the corresponding return mapping algorithm, (ii) the introduction of the resulting stress and constitutive elasto-plastic operator into the weak form of the IBVP, which is discretized in space by means of standard brick elements and solved through a standard incremental-iterative Newton-Raphson scheme, see Appendix.

4.1 Numerical Time Integration: General Return Mapping Algorithm

The classical backward Euler scheme is the most extensively used implicit algorithm for the integration of the evolution equations into elasto-plastic constitutive models. This numerical procedure is carried out at integration point level within a standard nonlinear FE code.

The basic integration scheme comprises two fundamental stages: (1) an initial elastic predictor phase, and (2) a subsequent corrector step using a general return mapping [14, 27]. Let us consider a time interval $[t_n, t_{n+1}]$, with $t \in \mathbb{R}_+$, where t_n and $t_{n+1}^{(i)}$ identify the previously converged time step and the current prospective time step at the global FE Newton-Raphson iteration i , respectively. In the sequel, the superscript i is omitted in order to alleviate the notation. Additionally, we assume that all variables of the problem at t_n are known, denoting the incremental time step as $\Delta t = t_{n+1}^{(i)} - t_n$. According to this scheme, the temporal rates of the plastic deformation gradient and the equivalent plastic strain renders:

$$\dot{\mathbf{F}}^p = \frac{\mathbf{F}_{n+1}^p - \mathbf{F}_n^p}{\Delta t}; \quad \dot{\bar{\epsilon}}^p = \frac{\bar{\epsilon}_{n+1}^p - \bar{\epsilon}_n^p}{\Delta t}. \quad (43)$$

For time integration of the evolution equations (Sect. 3.4), the discrete incremental forms according to the backward Euler algorithm take the form:

$$\mathbf{F}_{n+1}^p = \mathbf{F}_n^p + \gamma_{n+1} \mathbf{n}_{g,n+1} \mathbf{F}_{n+1}^p, \quad (44)$$

$$\bar{\epsilon}_{n+1}^p = \bar{\epsilon}_n^p + \gamma_{n+1} \sqrt{\frac{2}{3}} \|\mathbf{n}_{g,n+1}\|, \quad (45)$$

$$f_{n+1} = f(\bar{\Sigma}_{s,n+1}, \mathbf{A}, \bar{\epsilon}_{n+1}^p) = 0, \quad (46)$$

where γ_{n+1} identifies the plastic multiplier.

To start the predictor-corrector procedure discussed above, within the predictor phase, initial purely elastic trial increment (denoted by the superscript ‘tr’ in the sequel) is assumed. Then, the trial elastic deformation gradient $\mathbf{F}_{n+1}^{e, \text{tr}}$ reads:

$$\mathbf{F}_{n+1}^{e, \text{tr}} = \mathbf{F}_{n+1} \mathbf{F}_n^{p-1}. \quad (47)$$

Accordingly, the following operators can be computed:

$$\mathbf{C}_{n+1}^{e,\text{tr}} = \mathbf{F}_{n+1}^{e,\text{trT}} \mathbf{F}_{n+1}^{e,\text{tr}}; \quad \mathbf{E}_{n+1}^{e,\text{tr}} = \frac{1}{2} [\mathbf{C}_{n+1}^{e,\text{tr}} - \mathbf{1}], \quad (48)$$

$$\bar{\mathbf{S}}_{n+1}^{\text{tr}} = \mathbb{C}^e : \mathbf{E}_{n+1}^{e,\text{tr}}; \quad \bar{\Sigma}_{n+1}^{\text{tr}} = \mathbf{C}_{n+1}^{e,\text{tr}} \bar{\mathbf{S}}_{n+1}^{\text{tr}}. \quad (49)$$

Then, the trial elastic deformation gradient renders:

$$\mathbf{F}_{n+1}^e = \mathbf{F}_{n+1}^{e,\text{tr}} (\mathbf{1} - \gamma_{n+1} \mathbf{n}_{g,n+1}). \quad (50)$$

The corresponding trial yield function reads:

$$f_{n+1}^{\text{tr}} (\bar{\Sigma}_{s,n+1}^{\text{tr}}, \mathbf{A}, \bar{\varepsilon}_{n+1}^{p,\text{tr}}) = \frac{1}{2} \bar{\Sigma}_{s,n+1}^{\text{tr}} : \mathbb{K}_{n+1}^{\text{tr}} : \bar{\Sigma}_{s,n+1}^{\text{tr}} + \mathbf{L}_{n+1}^{\text{tr}} : \bar{\Sigma}_{s,n+1}^{\text{tr}} - 1 \leq 0, \quad (51)$$

where the operators \mathbb{K}^{tr} and \mathbf{L}^{tr} depend on the parameters $\zeta_i^{\text{tr}} = \zeta_i (\bar{\varepsilon}_{n+1}^{p,\text{tr}})$, ($i = 1, \dots, 6$).

If the predictor elastic trial state lies within the elastic domain \mathbb{E} , i.e. $f_{n+1}^{\text{tr}} \leq 0$ (where we omit the explicit dependencies), this state is a solution of the constitutive problem stated above. Conversely, a plastic corrector step is required for $f_{n+1}^{\text{tr}} > 0$, which is constructed as follows:

$$\mathbf{F}_{n+1}^e = \mathbf{F}_{n+1}^{e,\text{tr}} (\mathbf{1} - \gamma_{n+1} \mathbf{n}_{g,n+1}), \quad (52)$$

$$\bar{\varepsilon}_{n+1}^p = \bar{\varepsilon}_n^p + \gamma_{n+1} \sqrt{\frac{2}{3}} \|\mathbf{n}_{g,n+1}\|, \quad (53)$$

$$f_{n+1} = f (\bar{\Sigma}_{s,n+1}, \mathbf{A}, \bar{\varepsilon}_{n+1}^p) = 0, \quad (54)$$

where Eq. (54) stands for the yield criterion. Eqs. (52)–(54) identifies a discrete system of 11 nonlinear equations with 11 unknowns, which are solved simultaneously using a standard local Newton-Raphson procedure at integration point level. Thus, the corresponding residual equations $\mathbf{R}_{n+1} = \{\mathbf{R}_{\mathbf{F}_{n+1}^e}, \mathbf{R}_{\bar{\varepsilon}_{n+1}^p}, \mathbf{R}_{f_{n+1}}\}$ are arranged as follows:

$$\mathbf{R}_{\mathbf{F}_{n+1}^e} = \mathbf{F}_{n+1}^e - \mathbf{F}_{n+1}^{e,\text{tr}} (\mathbf{1} - \gamma_{n+1} \mathbf{n}_{g,n+1}) = \mathbf{0}, \quad (55)$$

$$\mathbf{R}_{\bar{\varepsilon}_{n+1}^p} = \bar{\varepsilon}_{n+1}^p - \left(\bar{\varepsilon}_n^p + \gamma_{n+1} \sqrt{\frac{2}{3}} \|\mathbf{n}_{g,n+1}\| \right) = 0, \quad (56)$$

$$\mathbf{R}_{f_{n+1}} = f_{n+1} = f (\bar{\Sigma}_{s,n+1}, \mathbf{A}, \bar{\varepsilon}_{n+1}^p) = 0, \quad (57)$$

which are solved for the variables $\chi_{n+1} = \{\mathbf{F}_{n+1}^e, \bar{\varepsilon}_{n+1}^p, \gamma_{n+1}\}$. The linearization of the residual equations \mathbf{R}_{n+1} for the nonlinear solution procedure with respect to corresponding unknowns χ_{n+1} can be computed as follows:

$$\mathbf{R}_{n+1}(\boldsymbol{\chi}_{n+1}^{k+1}) := \mathbf{R}_{n+1}(\boldsymbol{\chi}_{n+1}^k) + \mathbf{J}(\boldsymbol{\chi}_{n+1}^k) [\boldsymbol{\chi}_{n+1}^{k+1} - \boldsymbol{\chi}_{n+1}^k] = \mathbf{0}, \quad (58)$$

where the superscript k identifies the Newton-Raphson iteration index corresponding to the plastic corrector step of the present procedure. The Jacobian \mathbf{J} matrix takes the form:

$$\mathbf{J} = \begin{bmatrix} \frac{\partial \mathbf{R}_{\mathbf{F}^e}}{\partial \mathbf{F}^e} & \frac{\partial \mathbf{R}_{\mathbf{F}^e}}{\partial \bar{\epsilon}} & \frac{\partial \mathbf{R}_{\mathbf{F}^e}}{\partial \gamma} \\ \frac{\partial \mathbf{R}_{\bar{\epsilon}}}{\partial \mathbf{F}^e} & \frac{\partial \mathbf{R}_{\bar{\epsilon}}}{\partial \bar{\epsilon}} & \frac{\partial \mathbf{R}_{\bar{\epsilon}}}{\partial \gamma} \\ \frac{\partial \mathbf{R}_f}{\partial \mathbf{F}^e} & \frac{\partial \mathbf{R}_f}{\partial \bar{\epsilon}} & \frac{\partial \mathbf{R}_f}{\partial \gamma} \end{bmatrix}. \quad (59)$$

The increment of the unknowns can be computed as:

$$\Delta \boldsymbol{\chi}_{n+1}^{k+1} := \boldsymbol{\chi}_{n+1}^{k+1} - \boldsymbol{\chi}_{n+1}^k = -\mathbf{J}^{-1}(\boldsymbol{\chi}_{n+1}^k) \mathbf{R}_{n+1}(\boldsymbol{\chi}_{n+1}^k), \quad (60)$$

where the initial values for the plastic corrector procedure correspond to the results of the elastic predictor phase:

$$\boldsymbol{\chi}_{n+1}^{k=0} = \begin{bmatrix} \mathbf{F}_{n+1}^{e, \text{tr}} \\ \bar{\epsilon}_n \\ 0 \end{bmatrix}. \quad (61)$$

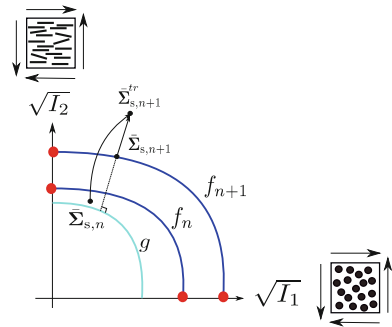
A representation of the current return mapping algorithm is shown in Fig. 6.

The closed form of the derivatives in Eq. (59) is outlined in the sequel. Thus, if $\mathbf{F}^e = \mathbf{F}^{e, \text{tr}}(\mathbf{1} - \gamma \mathbf{n}_g)$, the increment of the elastic part of the deformation gradient $\Delta \mathbf{F}^e$ yields:

$$\Delta \mathbf{F}^e = \mathbf{F}^{e, \text{tr}} \left(-\Delta \gamma \mathbf{n}_g - \gamma \frac{\partial \mathbf{n}_g}{\partial \mathbf{F}^e} : \Delta \mathbf{F}^e - \gamma \frac{\partial \mathbf{n}_g}{\partial \bar{\epsilon}} \Delta \bar{\epsilon} \right). \quad (62)$$

Consequently, the entries of the first row of \mathbf{J} can be expressed as:

Fig. 6 Return mapping algorithm: graphical description in the invariant space



$$\frac{\partial \mathbf{R}_{\mathbf{F}^e}}{\partial \mathbf{F}^e} = \mathbb{V}^*, \quad (63)$$

with

$$\mathbb{V}^* \Rightarrow \mathbb{V}_{ijkl}^* = \left(\delta_{ik}\delta_{jl} + \gamma \mathbf{F}_{im}^{e,\text{tr}} \frac{\partial \mathbf{n}_{g,mj}}{\mathbf{F}_{kl}^e} \right). \quad (64)$$

Furthermore, it is noting that:

$$\frac{\partial \mathbf{R}_{\mathbf{F}^e}}{\partial \bar{\varepsilon}^p} = 0; \quad \frac{\partial \mathbf{R}_{\mathbf{F}^e}}{\partial \gamma} = \mathbf{F}^{e,\text{tr}} \mathbf{n}_g. \quad (65)$$

Therefore, the increment of the equivalent plastic strain $\Delta \bar{\varepsilon}^p$ reads:

$$\Delta \bar{\varepsilon}^p = \sqrt{\frac{2}{3}} \Delta \gamma \|\mathbf{n}_g\| + \sqrt{\frac{2}{3}} \gamma \frac{\partial \|\mathbf{n}_g\|}{\partial \mathbf{F}^e} : \Delta \mathbf{F}^e. \quad (66)$$

Then, the corresponding entries of the second row of \mathbf{J} renders:

$$\frac{\partial \mathbf{R}_{\bar{\varepsilon}^p}}{\partial \mathbf{F}^e} = -\sqrt{\frac{2}{3}} \gamma \frac{\partial \|\mathbf{n}_g\|}{\partial \mathbf{F}^e}, \quad (67)$$

where

$$\frac{\partial \|\mathbf{n}_g\|}{\partial \mathbf{F}^e} = \frac{\mathbf{n}_g}{\|\mathbf{n}_g\|} : \frac{\partial \mathbf{n}_g}{\partial \mathbf{F}^e}. \quad (68)$$

Moreover, since $\mathbf{n}_g = \mathbb{M} : \bar{\boldsymbol{\Sigma}}_s$, this leads:

$$\frac{\partial \mathbf{n}_g}{\partial \mathbf{F}^e} = \mathbb{M} : \frac{\partial \bar{\boldsymbol{\Sigma}}_s}{\partial \mathbf{F}^e} \Rightarrow \left(\frac{\partial \mathbf{n}_g}{\partial \mathbf{F}^e} \right)_{ijkl} = \mathbb{M}_{ijab} \left(\frac{\partial \bar{\boldsymbol{\Sigma}}_s}{\partial \mathbf{F}^e} \right)_{abkl}, \quad (69)$$

where

$$\begin{aligned} \frac{\partial \bar{\boldsymbol{\Sigma}}_s}{\partial \mathbf{F}^e} &= \frac{1}{2} \frac{\partial (\bar{\boldsymbol{\Sigma}} + \bar{\boldsymbol{\Sigma}}^T)}{\partial \mathbf{F}^e} \Rightarrow \left(\frac{\partial \bar{\boldsymbol{\Sigma}}_s}{\partial \mathbf{F}^e} \right)_{ijkl} = \frac{1}{2} \mathbb{C}_{imkl}^* \bar{\mathbf{S}}_{mj} + \frac{1}{2} \mathbb{C}_{mjkl}^* \bar{\mathbf{S}}_{im} + \\ &\frac{1}{4} \mathbb{C}_{im}^e \mathbb{C}_{mjab}^e \mathbb{C}_{abkl}^* + \frac{1}{4} \mathbb{C}_{mj}^e \mathbb{C}_{imab}^e \mathbb{C}_{abkl}^*. \end{aligned} \quad (70)$$

In index notation yields:

$$\mathbb{C}^* \Rightarrow \mathbb{C}_{ijkl}^* = \left(\frac{\partial \mathbb{C}^e}{\partial \mathbf{F}^e} \right)_{ijkl} = \delta_{il} \mathbf{F}_{kj}^e + \delta_{jl} \mathbf{F}_{ki}^e. \quad (71)$$

Operating in a similar way:

$$\frac{\partial \mathbf{R}_{\bar{\varepsilon}^p}}{\partial \bar{\varepsilon}^p} = \mathbf{1}; \quad \frac{\partial \mathbf{R}_{\bar{\varepsilon}^p}}{\partial \gamma} = -\sqrt{\frac{2}{3}} \|\mathbf{n}_g\|. \quad (72)$$

Finally, the increment of the yield function Δf can be computed as:

$$\Delta f = \frac{\partial f}{\partial \mathbf{F}^e} : \Delta \mathbf{F}^e + \frac{\partial f}{\partial \bar{\varepsilon}^p} \Delta \bar{\varepsilon} + \frac{\partial f}{\partial \gamma} \Delta \gamma = 0. \quad (73)$$

Thus, the corresponding derivatives read (which concern entries of the third row of \mathbf{J}) yield:

$$\frac{\partial f}{\partial \mathbf{F}^e} = (\mathbb{K} : \bar{\boldsymbol{\Sigma}}_s + \mathbf{L}) : \frac{\partial \bar{\boldsymbol{\Sigma}}_s}{\partial \mathbf{F}^e}, \quad (74)$$

$$\frac{\partial f}{\partial \bar{\varepsilon}^p} = \frac{1}{2} \bar{\boldsymbol{\Sigma}}_s : \frac{\partial \mathbb{K}}{\partial \bar{\varepsilon}^p} : \bar{\boldsymbol{\Sigma}}_s + \frac{\partial \mathbf{L}}{\partial \bar{\varepsilon}^p} : \bar{\boldsymbol{\Sigma}}_s. \quad (75)$$

This novel material model is implemented into extended versions of the FE code FEAP and ABAQUS through user-defined material models, which operate at integration point level.

4.2 Algorithmic-Consistent Tangent Moduli

For fully implicit FE computations, the calculation of the tangential stiffness matrix at element level requires the derivation of the algorithmic tangent moduli which guarantees the quadratic convergence along the incremental-iterative solution process. We commence the derivation through the exploitation of Eq. (52). Accordingly, this results in:

$$\mathbf{F}^e = \mathbf{F}^{e,\text{tr}} (\mathbf{1} - \gamma \mathbf{n}_g) = \mathbf{F}^{e,\text{tr}} \mathbf{F}_*^p; \quad \text{with} \quad \mathbf{F}_*^{p-1} \mathbf{F}_n^p = \mathbf{F}^p. \quad (76)$$

Then, the incremental form of the plastic counterpart of the deformation gradient $\Delta \mathbf{F}_*^p$ renders:

$$\Delta \mathbf{F}_*^p = -\Delta \gamma \mathbf{n}_g - \gamma \frac{\partial \mathbf{n}_g}{\partial \vartheta} \Delta \vartheta - \gamma \frac{\partial \mathbf{n}_g}{\partial \mathbf{F}^e} : \Delta \mathbf{F}^e. \quad (77)$$

The increment of the elastic part of the deformation gradient can be expressed as:

$$\Delta \mathbf{F}^e = \Delta \mathbf{F} \mathbf{F}^{p-1} - \Delta \gamma \mathbf{F}^{e,\text{tr}} \mathbf{n}_g - \gamma \mathbf{F}^{e,\text{tr}} \frac{\partial \mathbf{n}_g}{\partial \mathbf{F}^e} : \Delta \mathbf{F}^e, \quad (78)$$

and the consistency condition renders:

$$\Delta f = \frac{\partial f}{\partial \mathbf{F}^e} : \Delta \mathbf{F}^e + \frac{\partial f}{\partial \bar{\varepsilon}^p} \Delta \bar{\varepsilon}^p = 0. \quad (79)$$

with

$$\Delta \bar{\varepsilon}^p = \sqrt{\frac{2}{3}} \Delta \gamma \|\mathbf{n}_g\| + \sqrt{\frac{2}{3}} \gamma \frac{\partial \|\mathbf{n}_g\|}{\partial \mathbf{F}^e} : \Delta \mathbf{F}^e. \quad (80)$$

The increment of the yield function takes the form:

$$\Delta f = \left(\frac{\partial f}{\partial \bar{\varepsilon}^p} \sqrt{\frac{2}{3}} \|\mathbf{n}_g\| \right) \Delta \gamma + \left(\frac{\partial f}{\partial \bar{\varepsilon}^p} \sqrt{\frac{2}{3}} \gamma \frac{\partial \|\mathbf{n}_g\|}{\partial \mathbf{F}^e} + \frac{\partial f}{\partial \mathbf{F}^e} \right) : \Delta \mathbf{F}^e = 0. \quad (81)$$

Based on the previous expression, the increment of the plastic multiplier is computed as:

$$\Delta \gamma = - \underbrace{\frac{\frac{\partial f}{\partial \bar{\varepsilon}^p} \sqrt{\frac{2}{3}} \gamma \frac{\partial \|\mathbf{n}_g\|}{\partial \mathbf{F}^e} + \frac{\partial f}{\partial \mathbf{F}^e}}{\frac{\partial f}{\partial \bar{\varepsilon}^p} \sqrt{\frac{2}{3}} \|\mathbf{n}_g\|}}_{\frac{\partial \gamma}{\partial \mathbf{F}^e}} : \Delta \mathbf{F}^e = \frac{\partial \gamma}{\partial \mathbf{F}^e} : \Delta \mathbf{F}^e. \quad (82)$$

Based on the previous derivations, $\Delta \mathbf{F}_*^p$ yields:

$$\Delta \mathbf{F}_*^p = - \underbrace{\left(\mathbf{n}_g \otimes \frac{\partial \gamma}{\partial \mathbf{F}^e} + \gamma \frac{\partial \mathbf{n}_g}{\partial \mathbf{F}^e} \right)}_{\mathbb{H}^p} : \Delta \mathbf{F}^e = \mathbb{H}^p : \Delta \mathbf{F}^e. \quad (83)$$

To accomplish the following steps, recalling $\bar{\mathbb{I}} \Rightarrow \bar{\mathbb{I}}_{ijkl} = \delta_{ik} \delta_{jl}$, we define:

$$\mathbb{N} = \bar{\mathbb{I}} + \gamma \mathbf{F}^{e, \text{tr}} \frac{\partial \mathbf{n}_g}{\partial \mathbf{F}^e}; \quad \mathbb{N}^* = \mathbb{N} + (\mathbf{F}^{e, \text{tr}} \mathbf{n}_g) \otimes \frac{\partial \gamma}{\partial \mathbf{F}^e}. \quad (84)$$

Inserting Eq. (82) into Eq. (78) yields:

$$\mathbb{N} : \Delta \mathbf{F}^e = \Delta \mathbf{F} \mathbf{F}^{p-1} - \mathbf{F}^{e, \text{tr}} \mathbf{n}_g \left(\frac{\partial \gamma}{\partial \mathbf{F}^e} : \Delta \mathbf{F}^e \right). \quad (85)$$

Then, it is possible to obtain:

$$\Delta \mathbf{F}^e = \mathbb{N}^{*-1} : (\Delta \mathbf{F} \mathbf{F}^{p-1}). \quad (86)$$

An additional computation that should be performed is the increment of $\Delta \bar{\mathbf{S}}$:

$$\Delta \bar{\mathbf{S}} = \left(\frac{\partial \bar{\mathbf{S}}}{\partial \mathbf{E}^e} : \frac{\partial \mathbf{E}^e}{\partial \mathbf{F}^e} \right) : \Delta \mathbf{F}^e = \underbrace{\left(\mathbb{C}^e : \frac{\partial \mathbf{E}^e}{\partial \mathbf{F}^e} \right)}_{\mathbb{C}_{\mathbf{F}}^e} : \Delta \mathbf{F}^e, \quad (87)$$

Then, $\Delta \mathbf{F}^{p-1}$ takes the form:

$$\Delta \mathbf{F}^{p-1} = \Delta (\mathbf{F}_n^{p-1} \mathbf{F}_*^p) = \mathbf{F}_n^{p-1} \Delta \mathbf{F}_*^p, \quad (88)$$

and correspondingly:

$$\Delta \mathbf{F}^{p-T} = \Delta (\mathbf{F}_*^p \mathbf{F}_n^{p-T}) = \Delta \mathbf{F}_*^p \mathbf{F}_n^{p-T}. \quad (89)$$

The increment of the first Piola-Kirchhoff stress tensor ($\mathbf{P} := \mathbf{FS}$) can be computed as:

$$\Delta \mathbf{P} = \Delta (\mathbf{FS}), \quad (90)$$

with \mathbf{P} standing for the first Piola-Kirchhoff stress tensor. Expanding the previous expression yields:

$$\Delta (\mathbf{FS}) = \Delta \mathbf{FS} + \mathbf{F} \Delta \mathbf{S} = \Delta \mathbf{F} (\mathbf{F}^{p-1} \tilde{\mathbf{S}} \mathbf{F}^{p-T}) + \mathbf{F} \Delta (\mathbf{F}^{p-1} \tilde{\mathbf{S}} \mathbf{F}^{p-T}), \quad (91)$$

where

$$\Delta (\mathbf{FS}) = \Delta \mathbf{F} (\mathbf{F}^{p-1} \tilde{\mathbf{S}} \mathbf{F}^{p-T}) + \mathbf{F} \Delta \mathbf{F}^{p-1} \tilde{\mathbf{S}} \mathbf{F}^{p-T} + \mathbf{F} \mathbf{F}^{p-1} \Delta \tilde{\mathbf{S}} \mathbf{F}^{p-T} + \mathbf{F} \mathbf{F}^{p-1} \tilde{\mathbf{S}} \Delta \mathbf{F}^{p-T}, \quad (92)$$

and

$$\Delta \mathbf{F}^{p-T} = \Delta (\mathbf{F}_*^p \mathbf{F}_n^{p-T}) = \Delta \mathbf{F}_*^p \mathbf{F}_n^{p-T}. \quad (93)$$

Eq. (92) can be expanded as:

$$\begin{aligned} \Delta (\mathbf{FS}) = & \Delta \mathbf{F} (\mathbf{F}^{p-1} \tilde{\mathbf{S}} \mathbf{F}^{p-T}) + \\ & \mathbf{F} \mathbf{F}_n^{p-1} (\mathbb{H}^p : \Delta \mathbf{F}^e) \tilde{\mathbf{S}} \mathbf{F}^{p-T} + \\ & \mathbf{F} \mathbf{F}^{p-1} (\mathbb{C}_{\mathbf{F}}^e : \Delta \mathbf{F}^e) \mathbf{F}^{p-T} + \\ & \mathbf{F} \mathbf{F}^{p-1} \tilde{\mathbf{S}} (\mathbb{H}^p : \Delta \mathbf{F}^e) \mathbf{F}_n^{p-T}. \end{aligned} \quad (94)$$

Inserting the results from Eq. (86) into Eq. (93) yields:

$$\begin{aligned} \Delta (\mathbf{FS}) = & \Delta \mathbf{F} (\mathbf{F}^{p-1} \tilde{\mathbf{S}} \mathbf{F}^{p-T}) + \\ & \mathbf{F} \mathbf{F}_n^{p-1} (\mathbb{H}^p : (\mathbb{N}^{*-1} : (\Delta \mathbf{F} \mathbf{F}^{p-1}))) \tilde{\mathbf{S}} \mathbf{F}^{p-T} + \\ & \mathbf{F} \mathbf{F}^{p-1} (\mathbb{C}_{\mathbf{F}}^e : (\mathbb{N}^{*-1} : (\Delta \mathbf{F} \mathbf{F}^{p-1}))) \mathbf{F}^{p-T} + \\ & \mathbf{F} \mathbf{F}^{p-1} \tilde{\mathbf{S}} (\mathbb{H}^p : (\mathbb{N}^{*-1} : (\Delta \mathbf{F} \mathbf{F}^{p-1}))) \mathbf{F}_n^{p-T}, \end{aligned} \quad (95)$$

which in index notation reads:

$$\Delta(\mathbf{FS})_{ij} = \left(\delta_{ik} \mathbf{F}_{ln}^{p-1} \bar{\mathbf{S}}_{ns} \mathbf{F}_{sj}^{p-T} \right) \Delta \mathbf{F}_{kl} + \quad (96)$$

$$\left(\mathbf{F}_{im} \mathbf{F}_{n,mx}^{p-1} \mathbb{H}_{xnab}^p \mathbb{N}_{abky}^{*-1} \mathbf{F}_{ly}^{p-1} \bar{\mathbf{S}}_{ns} \mathbf{F}_{sj}^{p-T} \right) \Delta \mathbf{F}_{kl} + \quad (97)$$

$$\left(\mathbf{F}_{im} \mathbf{F}_{mn}^{p-1} \mathbb{C}_{\mathbf{F},nsab}^e \mathbb{N}_{abky}^{*-1} \mathbf{F}_{ly}^{p-1} \mathbf{F}_{sj}^{p-T} \right) \Delta \mathbf{F}_{kl} + \quad (98)$$

$$\left(\mathbf{F}_{im} \mathbf{F}_{mn}^{p-1} \bar{\mathbf{S}}_{ns} \mathbb{H}_{sxab}^p \mathbb{N}_{abky}^{*-1} \mathbf{F}_{ly}^{p-1} \mathbf{F}_{n,xj}^{p-T} \right) \Delta \mathbf{F}_{kl}. \quad (99)$$

Finally, in condensed format, it can be expressed:

$$\Delta(\mathbf{FS}) = \mathbb{C}^{ep} : \Delta \mathbf{F} \Rightarrow \Delta(\mathbf{FS})_{ij} = \mathbb{C}_{ijkl}^{ep} \Delta \mathbf{F}_{kl}, \quad (100)$$

which closed form in index notation renders:

$$\begin{aligned} \mathbb{C}^{ep} \Rightarrow \mathbb{C}_{ijkl}^{ep} = & \delta_{ik} \mathbf{F}_{ln}^{p-1} \bar{\mathbf{S}}_{ns} \mathbf{F}_{sj}^{p-T} + \\ & \mathbf{F}_{im} \mathbf{F}_{n,mx}^{p-1} \mathbb{H}_{xnab}^p \mathbb{N}_{abky}^{*-1} \mathbf{F}_{ly}^{p-1} \bar{\mathbf{S}}_{ns} \mathbf{F}_{sj}^{p-T} + \\ & \mathbf{F}_{im} \mathbf{F}_{mn}^{p-1} \mathbb{C}_{\mathbf{F},nsab}^e \mathbb{N}_{abky}^{*-1} \mathbf{F}_{ly}^{p-1} \mathbf{F}_{sj}^{p-T} + \\ & \mathbf{F}_{im} \mathbf{F}_{mn}^{p-1} \bar{\mathbf{S}}_{ns} \mathbb{H}_{sxab}^p \mathbb{N}_{abky}^{*-1} \mathbf{F}_{ly}^{p-1} \mathbf{F}_{n,xj}^{p-T}, \end{aligned} \quad (101)$$

To finish the current derivations, the following computations are also required:

$$\frac{\partial \|\mathbf{n}_g\|}{\partial \mathbf{F}^e} = \frac{\partial \|\mathbf{n}_g\|}{\partial \mathbf{n}_g} : \frac{\partial \mathbf{n}_g}{\partial \mathbf{F}^e} = \frac{\mathbf{n}_g}{\|\mathbf{n}_g\|} : \frac{\partial \mathbf{n}_g}{\partial \mathbf{F}^e}. \quad (102)$$

Given that $\mathbf{n}_g = \mathbb{M} : \bar{\mathbf{\Sigma}}_s$, so:

$$\Delta \mathbf{n}_g = \mathbb{M} : \Delta \bar{\mathbf{\Sigma}}_s = \mathbb{M} : \frac{\partial \bar{\mathbf{\Sigma}}_s}{\partial \mathbf{F}^e} : \Delta \mathbf{F}^e, \quad (103)$$

and therefore:

$$\frac{\partial \mathbf{n}_g}{\partial \mathbf{F}^e} = \mathbb{M} : \frac{\partial \bar{\mathbf{\Sigma}}_s}{\partial \mathbf{F}^e}. \quad (104)$$

5 Applications

In this section, several numerical results are presented in order to examine the performance of the constitutive model herein developed. The applications henceforth presented are: (i) a verification case concerning dog-bone specimen types under tensile loading with different preferential fibre orientations (Sect. 5.1), and (ii) a validation through a three-point bending test (Sect. 5.2).

5.1 Model Verification and Validation

In the first application, dog-bone specimen-types with different preferential fiber orientations are subjected to uniform tensile loading. These specimens are manufactured from the short fiber-reinforced thermoplastic PA6GF-30 and were experimentally investigated at the Institute of Forming Technology and Machines (IFUM, Hannover) [10]. The corresponding mechanical properties are given in Table 1. Note that averaged fiber distribution over the cross section of the specimen is considered complying with the so-called Equivalent Single Layer (ESL) approach [23].

The geometry of the specimen is shown in Fig. 7a, identifying the zero-degree reference material orientation. The specimen is discretized using 4860 first-order solid

Table 1 PA6GF-30: mechanical properties

E_{11} (MPa)	E_{22} (MPa)	G_{12} (MPa)	ν_{12}	ν_{23}
7893.550	3348.17	1800.94	0.23	0.62

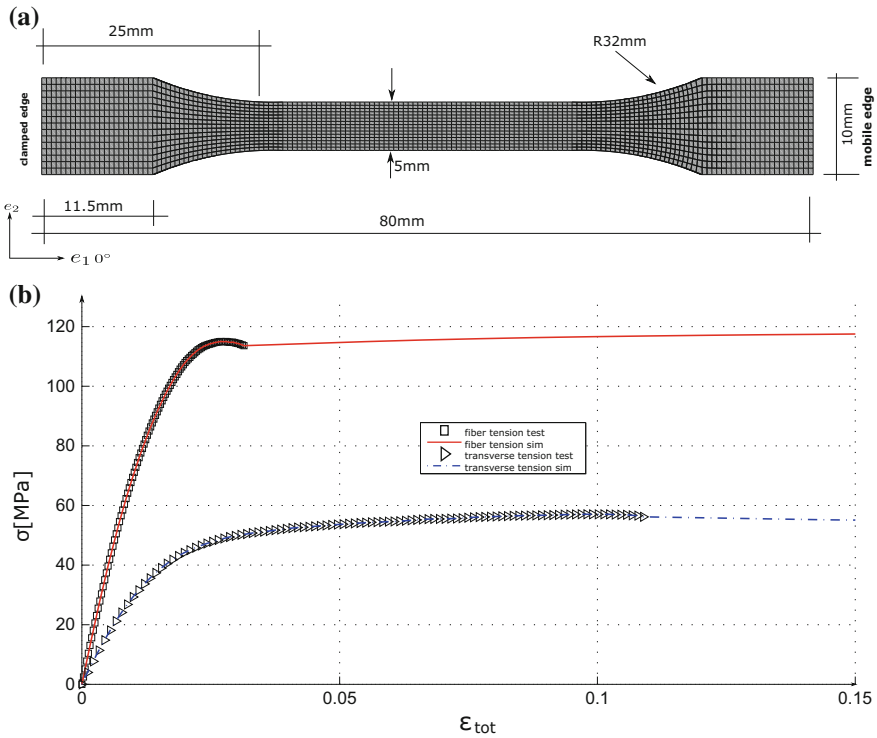


Fig. 7 Dog-bone specimens PA6GF-30 under uniaxial loading conditions. **a** Specimen definition **b** Experimental–numerical correlation for different preferential fiber orientations (0° and 90°)

elements. To reproduce the experimental conditions, the following boundary conditions are defined [7]: (i) fully restrained displacements at the clamped edge, and (ii) constrained displacements at the loaded edge, except the longitudinal displacement coinciding with the 0°-direction.

The initial yielding parameters, ζ_i , are reported in Table 2, whereas the plastic potential parameters l_i are listed in Table 3. The geometry of the specimen is shown in Fig. 7a, identifying the zero-degree reference material orientation. Fig. 8 depicts the convex form of the yield surface.

Figures 7b shows the experimental–numerical correlation between the current simulations and the data reported in [10], whereby a satisfactory agreement can be observed.

Table 2 PA6GF-30: initial yielding parameters ζ_i

ζ_1	ζ_2	ζ_3	ζ_4	ζ_5	ζ_6
2.648×10^{-4}	2.648×10^{-4}	3.272×10^{-3}	2.523×10^{-5}	1.338×10^{-3}	2.588×10^{-4}

Table 3 PA66GF-35: plastic potential parameters l_i

l_1	l_2
1.0	-17.684

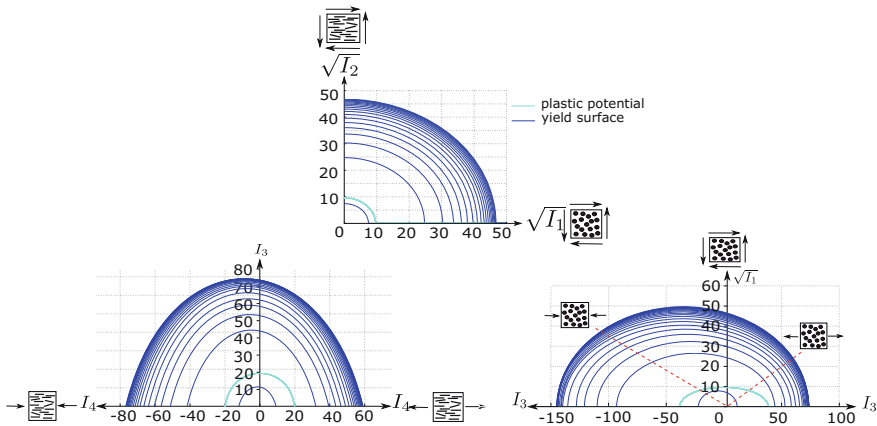


Fig. 8 PA6GF30: Characterization of the yield surface and plastic potential

Table 4 PA6GF-30: Mechanical properties

E_{11} (MPa)	E_{22} (MPa)	G_{12} (MPa)	ν_{12}	ν_{23}
5211.43	2262.86	1601.7	0.39	0.6

Table 5 PA6GF-30: initial yielding parameters ζ_i

ζ_1	ζ_2	ζ_3	ζ_4	ζ_5	ζ_6
4.521×10^{-4}	4.521×10^{-4}	6.624×10^{-3}	9.429×10^{-5}	3.899×10^{-3}	2.196×10^{-4}

Table 6 PA6GF-30: plastic potential parameters ι_i

ι_1	ι_2
1.0	-17.684

5.2 Structural Application: Three-Point Bending Test

The second application studied concerns the 3-point bending test previously reported in [26]. In particular, we restrict our analysis to the case of a loading velocity of 1.0 m/s to prevent incongruities with the quasi-static character of the current formulation. The material properties corresponding to the present case are listed in Table 4, whereas the plastic data are reported in Tables 5 and 6, respectively, complying with the ISO standard value corresponding to this material. Similarly to the previous application, we exploit the ESL approach to compute the corresponding mechanical properties over the plate thickness. This example is of special interest to characterize the mechanical performance and to trigger the fiber orientation along the loading procedure. Therefore, this application is herein used to assess the proposed formulation.

Figure 9a shows the geometric description of the current application, identifying the preferential fibre orientation with the longitudinal direction of the specimen and with the following geometric dimensions: (i) length $L = 50$ mm, (ii) width $B = 5$ mm, and (iii) thickness $t = 2$ mm. The plate is discretized using 7200 first-order solid elements. The pin for the loading application is meshed using 2100 elements with the same interpolation order and setting very high mechanical properties to prevent its deformation. The computations are performed prescribing the downward vertical displacement at the central pin equal to 9 mm using 1000 equal pseudo-time increments. It should be noted that ABAQUS simulations are performed using automatic time stepping. Figure 9b shows the longitudinal stress distribution over the plate thickness, featuring a nonuniform distribution over the thickness due to the imposed loading.

Simulations are conducted imposing a prescribed vertical displacement downwards at the central pin equal to 9 mm, see Fig. 9a ,b. In each increment, the global solution scheme is employed. Figure 9b shows the stress distribution due to the prescribed loading, where, as expected, a nonuniform strain distribution over the plate

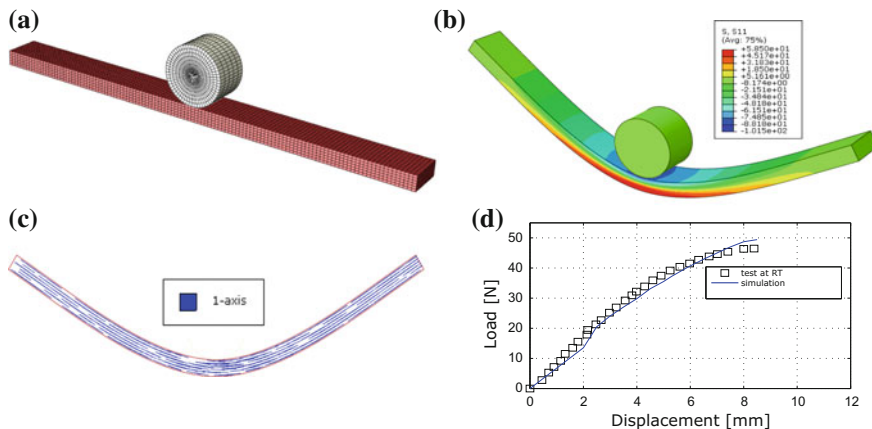


Fig. 9 Three-point bending test of PA6GF-30. **a** Specimen definition **b** Stress distribution **c** Mapping of the preferential material direction after the computation **d** Experimental–numerical correlation

thickness is estimated. Figure 9c displays the preferential material orientation along the thickness direction, whereby the mapping of the fibre alignments along the deformation process is mapped.

Finally, Fig. 9d shows the experimental-numerical correlation corresponding to the load–central displacement evolution curve of the application. In this graph, the experimental data are represented through discrete square symbols, whereas the simulation results are plotted using a solid line. Examining this evolution, it is interesting to see that a very good correlation is obtained along the whole loading procedure. In this respect, note that the mechanical performance of the systems is characterized by an initial linear evolution followed by a subsequent stage where notable nonlinear effects become appreciable.

6 Concluding Remarks

In this investigation, a new elasto-plastic invariant-based finite strain anisotropic material model for SFRP composites has been presented. The proposed formulation is suitable for arbitrarily large elastic and plastic deformations, assuming plastic incompressibility.

On the theoretical side, the model incorporates a non-associate flow rule to characterize the plastic evolution, which relies on the multiplicative decomposition of the deformation gradient. The constitutive equations are derived in a thermodynamically consistent format. On the computational side, the current investigation provides a comprehensive presentation of the numerical treatment within the context of nonlinear FEM. In particular, a closed form of the algorithmic tangent moduli is derived.

The reliability of the current formulation has been examined by verification and validation examples, showing a very satisfactory level of accuracy with respect to the experimental data.

Finally, further research activities will comprise the application of the proposed formulation to hybrid metal-composite clinching manufacturing processes.

Acknowledgements The authors gratefully acknowledge the financial support of the German Research Foundation (DFG) through the program SPP 1640 (joining by plastic deformation) under the contract No. RO 706/6-2. JR is also grateful to the Spanish Ministry of Economy and Competitiveness (Projects MAT2015-71036-P and MAT2015-71309-P) and the Andalusian Government (Project of Excellence No. TEP-7093). AD gratefully acknowledges the support of Mr. and Mrs. Dean.

Appendix

This appendix addresses the weak formulation of the IBVP presented in Eq. (6) (Sect. 2), which represents the most convenient setting to formulate the corresponding numerical approximation based on FEM (Finite Element Method) through the exploitation of the standard Galerkin procedure.

Assume that the reference body boundary $\partial\mathcal{B}_0$ is subdivided into the disjointed parts $\partial\mathcal{B}_{0,u} \subset \partial\mathcal{B}_0$ and $\partial\mathcal{B}_{0,t} \subset \partial\mathcal{B}_0$, with $\partial\mathcal{B}_0 = \partial\mathcal{B}_{0,u} \cup \partial\mathcal{B}_{0,t}$ and $\partial\mathcal{B}_{0,u} \cap \partial\mathcal{B}_{0,t} = \emptyset$. As customary, appropriate boundary conditions must be defined in order to guarantee the well-posedness of the IBVP. The weak form of the balance of linear momentum reads:

$$\begin{aligned} G^u(\mathbf{u}, \delta\mathbf{u}) &= \int_{\mathcal{B}_0} (\text{DIV}[\mathbf{P}] + \tilde{\mathbf{Y}}) \delta\mathbf{u} dV = \int_{\mathcal{B}_0} (\text{DIV}[\delta\mathbf{u}\mathbf{P}] - \mathbf{P} : \nabla_{\mathbf{X}}\delta\mathbf{u} + \tilde{\mathbf{Y}}\delta\mathbf{u}) dV \\ &= \int_{\mathcal{B}_0} \mathbf{P} : \delta\mathbf{F} dV - \int_{\partial\mathcal{B}_0} \mathbf{T}\delta\mathbf{u} dA - \int_{\mathcal{B}_0} \tilde{\mathbf{Y}}\delta\mathbf{u} dV = G_{int}^u + G_{ext}^u = 0, \end{aligned} \quad (105)$$

where $\delta\mathbf{u}$ renders the virtual displacement and $\delta\mathbf{F} = \nabla_{\mathbf{X}}\delta\mathbf{u}$ and $\mathbf{T} = \mathbf{P}\mathbf{N}$ denotes the first Piola-Kirchhoff traction vector. Note that to achieve the present form of Eq. 105, the following rules are used:

$$\text{DIV}[\mathbf{P}] \delta\mathbf{u} = \text{DIV}[\delta\mathbf{u}\mathbf{P}] - \mathbf{P} : \nabla_{\mathbf{X}}\delta\mathbf{u}, \quad (106)$$

and the Gauss-Green theorem:

$$\int_{\mathcal{B}_0} \text{DIV}[\delta\mathbf{u}\mathbf{P}] dV = \int_{\partial\mathcal{B}_0} (\mathbf{P}\mathbf{N}) \delta\mathbf{u} dA. \quad (107)$$

The virtual internal work G_{int}^u and the virtual work of external actions G_{ext}^u are given by:

$$G_{int}^u(\mathbf{u}, \delta\mathbf{u}) = \int_{\mathcal{B}_0} \mathbf{P} : \delta\mathbf{F} dV, \quad (108)$$

$$G_{ext}^u(\mathbf{u}, \delta\mathbf{u}) = - \int_{\partial\mathcal{B}_0} \mathbf{T}\delta\mathbf{u}dA - \int_{\mathcal{B}_0} \tilde{\mathbf{Y}}\delta\mathbf{u}dV. \quad (109)$$

The resulting set of nonlinear equations of the mechanical problem, Eq. 105, can be solved numerically through the use of the incremental and iterative Newton-Raphson solution scheme, which shows a quadratic convergence near the solution point. The consistent linearization of the given time integration algorithm, also called stress-update algorithm, leads to the derivation of the consistent tangent moduli, which describes in an incremental manner the stress sensitivity with respect to the deformation gradient increment. Following the directional derivative concept [16], the consistent linearization of Eq. 105 takes the following representation:

$$\text{Lin}[G^u(\bar{\mathbf{u}}, \delta\mathbf{u}, \Delta\mathbf{u})] = G^u(\bar{\mathbf{u}}, \delta\bar{\mathbf{u}}) + DG^u(\bar{\mathbf{u}}, \delta\mathbf{u}) \Delta\mathbf{u}. \quad (110)$$

In Eq. 105, the term $\mathbf{P} : \delta\mathbf{F}$ has to be linearized yielding:

$$\Delta(\mathbf{P} : \delta\mathbf{F}) = \Delta\mathbf{P} : \delta\mathbf{F}, \quad (111)$$

where $\Delta\mathbf{P}$ is derived in Sect. 4.2, with:

$$\Delta\mathbf{P} = \Delta(\mathbf{FS}) = \mathbb{C}^{ep} : \Delta\mathbf{F}, \quad (112)$$

where \mathbb{C}^{ep} denotes the algorithmic elasto-plastic constitutive operator.

References

1. Advani, S.G., Tucker, C.L.: The use of tensors to describe and predict fiber orientation in short fiber composites. *J. Rheol.* **31**, 751–784 (1987)
2. Advani, S.G., Talreja, R.: A continuum approach to determination of elastic properties of short fibre composites. *Mech. Compos. Mater.* **29**(2), 171–183 (1993)
3. Arif, M.F., Saintier, N., Meraghni, F., Fitoussi, J., Chemisky, Y., Robert, G.: Multiscale fatigue damage characterization in short glass fiber reinforced polyamide-66. *Comp. Part B* **61**, 55–65 (2014)
4. Bellenger, V., Tcharkhtchi, A., Castaing, P.: Thermal and mechanical fatigue of a PA66/glass fibers composite material. *Int. J. Fatigue* **28**(10), 1348–1352 (2006)
5. Bernasconi, A., Cosmi, F., Hine, P.J.: Analysis of fibre orientation distribution in short fibre reinforced polymers: a comparison between optical and tomographic methods. *Compos. Sci. Technol.* **72**(16), 2002–2008 (2012)
6. Boehler, J.P.: Applications of tensor functions in solid mechanics. In: *CISM Courses and Lectures*, vol. 292. Springer (1987)
7. Dean, A., Reinoso, J., Sahraee, S., Rolfes, R.: An invariant-based anisotropic material model for short fiber-reinforced thermoplastics: coupled thermo-plastic formulation. *Compos. Part A Appl. Sci. Manufact.* **90**, 186–199 (2016)
8. Dean, A., Sahraee, S., Reinoso, J., Rolfes, R.: Finite deformation model for short fiber reinforced composites: application to hybrid metal-composite clinching joints. *Compos. Struct.* **151**, 162–171 (2016)

9. Dean, A., Sahraee, S., Reinoso, J., Rolfes, R.: A New invariant-based thermo-plastic model for finite deformation analysis of short fibre reinforced composites: development and numerical aspects. *Compos. Part B Eng.* **125**, 241–258 (2017)
10. De Monte, M., Moosbugger, E., Quaresimin, M.: Influence of temperature and thickness on the off-axis behaviour of short glass fibre reinforced polyamide 6.6 Quasi-static loading. *Compos. Part A* **41**, 859–871 (2010)
11. De Monte, M., Moosbugger, E., Quaresimin, M.: Influence of temperature and thickness on the off-axis behaviour of short glass fibre reinforced polyamide 6.6 Cyclic loading. *Compos. Part A* **41**, 1368–79 (2010)
12. Eftekhari, M., Fatemi, A.: Tensile, creep and fatigue behaviors of short fiber reinforced polymer composites at elevated temperatures: a literature survey. *Fatigue Fract. Eng. Mater. Struct.* **38**, 1395 (2015)
13. Eidel, B., Gruttmann, F.: Elastoplastic orthotropy at finite strains: multiplicative formulation and numerical implementation. *Comput. Mater. Sci.* **28**, 732–742 (2003)
14. Eidel, B.: Anisotropic Inelasticity: Modelling, Simulation, Validation. Ph.D. Dissertation, Technischen Universität Darmstadt, Darmstadt, Germany (2004)
15. Feyel, F., Chaboche, J.-L.: FE2 multiscale approach for modelling the elastoviscoplastic behaviour of long fibre SiC/Ti composite materials, *Computer Meth. in Appl. Mech. Eng.* **183**, 309–330 (2000)
16. Holzapfel, G. A.: *Nonlinear Solid Mechanics*. Wiley (2000). ISBN: 978-0-471-82319-3
17. Lu, S.C.H., Pister, K.D.: Decomposition of deformation and representation of the free energy function for isotropic thermoelastic solids. *Int. J. Solids Struct.* **11**, 927–934 (1975)
18. Marco, Y., Le Saux, V., Jégou, L., Launay, A., Serrano, L., Raoult, I., Callot, S.: Dissipation analysis in SFRP structural samples: thermomechanical analysis and comparison to numerical simulations. *Int. J. Fatigue* **67**, 142–150 (2014)
19. Menzel, A., Steinmann, P.: On the spatial formulation of anisotropic multiplicative elastoplasticity. *Comput. Methods Appl. Mech. Eng.* **192**, 3431–3470 (2003)
20. Miehe, C., Apel, N., Lambrecht, M.: Anisotropic additive plasticity in the logarithmic strain space: modular kinematic formulation and implementation based on incremental minimization principles for standard materials. *Comput. Methods Appl. Mech. Eng.* **191**, 5383–5425 (2002)
21. Mlekusch, B.: Thermoelastic properties of short-fibre-reinforced thermoplastics. *Compos. Sci. Technol.* **59**, 911–923 (1999)
22. Reese, S.: Meso-macro modelling of fibre-reinforced rubber-like composites exhibiting large elastoplastic deformation. *Int. J. Solids Struct.* **40**(4), 951–980 (2003)
23. Reinoso, J., Blázquez, A.: Application and finite element implementation of 7-parameter shell element for geometrically nonlinear analysis of layered CFRP composites. *Compos. Struct.* **139**, 263–276 (2016)
24. Sansour, C., Karsaj, I., Soric, J.: On a formulation for anisotropic elastoplasticity at finite strains invariant with respect to the intermediate configuration. *J. Mech. Phys. Sol.* **55**, 2406–2426 (2007)
25. Schröder, J., Gruttmann, F., Löblein, J.: A simple orthotropic finite elastoplasticity model based on generalized stress strain measures. *Comput. Mech.* **30**, 48–64 (2002)
26. Schröpfer, J.: Spritzgussbauteile aus kurzfaserverstärkten Kunststoffen: Methoden der Charakterisierung und Modellierung zur nichtlinearen Simulation von statischen und crashrelevanten Lastfällen. Dissertation Technischen Universität Kaiserslautern (2011)
27. Simo, J.C., Miehe, C.: Associative coupled thermoplasticity at finite strains: Formulation numerical analysis and implementation. *Comput. Methods Appl. Mech. Eng.* **98**, 41–104 (1992)
28. Spahn, J., Andrä, H., Kabel, M., Müller, R.: A multiscale approach for modeling progressive damage of composite materials using fast Fourier transforms *Comput Method Appl. Mech. Eng.* **268**, 871–883 (2014)
29. Spencer, A.J.M.: Theory of invariants, In: Eringen, A.C. (Ed.), *Continuum Physics*, vol. 1, Academic Press, New York, 239–353 (1971)

30. Thi, T.B.N., Morioka, M., Yokoyama, A., Hamanaka, S., Yamashita, K., Nonomura, C.: Measurement of fiber orientation distribution in injection-molded short-glass- fiber composites using X-ray computed tomography. *J. Mater. Process. Technol.* **219**, 1–9 (2015)
31. Truesdell, C., Noll, W.: The nonlinear field theories of mechanics, In: Flügge, S. (Ed.) *Encyclopedia of Physics*, vol. III/3. Springer, Berlin (1965)
32. Vladimirov, I. N., Pietryga, M. P., Reese, S.: Anisotropic finite elastoplasticity with nonlinear kinematic and isotropic hardening and application to sheet metal forming. *Int. J. Plasticity*. 0749–6419, **26**, 659–687 (2010)
33. Vogler, M., Rolfes, R., Camanho, P.P.: Modeling the inelastic deformation and fracture of polymer composites part I: plasticity model. *Mech. Mater.* **59**, 50–64 (2013)
34. Zohdi, T., Wriggers, P.: Aspects of the computational testing of properties of microheterogeneous material samples. *Inter. J. Meth. Eng.* **50**, 2573–2599 (2001)